Terahertz Dielectric Metasurface for Reconfigurable Multifunctional Holographic Imaging with Dual-Mode Controlled by Graphene

Hui-Fen Huang * and Jian-Yuan Wang

Posted Date: 29 July 2024

doi: 10.20944/preprints202407.2254.v1

Keywords: terahertz; metasurface; holographic; graphene; reconfigurability

Article

Terahertz Dielectric Metasurface for Reconfigurable Multifunctional Holographic Imaging with Dual-Mode Controlled by Graphene

Hui-Fen Huang * and Jian-Yuan Wang

School of Electronic and Information Engineering, South China University of Technology, Guangzhou 510640, China

* Correspondence: huanghf@scut.edu.cn

Abstract: Metasurface constitutes one of the most promising technologies for holographic imaging; however, the work for terahertz (THz) metasurface holographic imaging is relatively limited. Here, we propose a THz dielectric geometric-propagation phase metasurface, which can operate dual-mode (reflection and transmission) and reconfigurable multifunctional holographic imaging. The dual-mode is realized by controlling the Fermi energy level (E_f) of the graphene integrated into the metasurface unit, and the reconfigurable three-channel holographic imaging in reflection or transmission mode are achieved by switching the feed polarization among left-handed circular polarization (LCP), right-handed circular polarization (RCP) and linear polarization (LP). The metasurface is designed based on the transmission mode, and a physical model for switching to the reflection mode is established. For the first time to the best of our knowledge, a reflection-transmission dynamic modulation THz holographic imaging metasurface has been developed. The holographic metasurface operates in transmission mode at E_f = 0.1 eV, and in reflection mode at E_f = 0.9 eV. Compared with recently published holographic imaging metasurfaces, the proposed metasurface offers the following advantages: high holographic efficiencies (42.5% to 49%), more holographic imaging channels, dynamic modulation dual-mode operations, and reconfigurability.

Keywords: terahertz; metasurface; holographic; graphene; reconfigurability

1. Introduction

Holography is an advanced imaging technology where image information can be reconstructed without a lens. It is an important tool for controlling wave fields and producing highly complex and customized field distributions. Since its invention, holography has been widely used to record and reconstruct all the information of an object, and has found applications in medical observation, virtual reality displays, sensing, data storage, security, secure printing [1,2], and secret sharing [3]. Recently, multiplexing techniques have been widely adopted to realize multiple holographic images or functionalities to increase the information capacity and make the optimum use of the space-bandwidth product. Particularly, with the advancement of computer-generated holograms, hologram generation can be done in an easier way through programming.

Metasurfaces offer flexible capabilities in manipulating the phase, amplitude, wavelength, and polarization of the incident wave. In addition, metasurfaces are capable of manipulating electromagnetic fields at the subwavelength scale, and enable holographic displays with higher resolution, wider field of view, and smaller geometry size [4]. Since a plasmonic metasurface for holography generation in 2013, metasurface-based holography has emerged as a vibrant research field [5]. Holographic multiplexing metasurfaces can record multiple images within the same spatial area, which increase information capacity while maintaining an ultrasmall footprint, subwavelength resolution, and larger field of view. So holographic multiplexing metasurfaces have received widely attention. Numerous studies have been conducted in the light frequency band: a single-layer LP metasurface for independently projecting different hologram images in transmission and reflection

 doi:10.20944/preprints202407.2254.v1

modes at the same frequency [6], a single-layer transmission metasurface generating multi-channel gray images by separately and independently controlling the amplitude and phase [7], a tri-channel single-layer transmission metasurface simultaneously recording a continuous grayscale nanoprinting image in the near field and projecting two independent holographic images in the far-field [8], an all-dielectric transmission single-layer metasurface generating polarization-multiplexed holographic images [9]. Significant advancements have also been achieved in the microwave frequency band: a single-layer reflective metasurface generating four-channel holographic images by simultaneous frequency and polarization multiplexing at 7.5 GHz and 13 GHz [10], a frequency-multiplexed single layered transmission metasurface for four-channel holography images at 7.2 GHz, 9.1 GHz, 10.9 GHz, and 15.2 GHz [11], a full-space single-layer encoding metasurface independently manipulating the images 'F' and 'H' in transmission or reflection mode based on polarization multiplexing at 10GHz [12], reconfigurable holographic images achieved by switching the transmission metasurface shape from planar (for the letter 'Z' image, 14.8-15.0 GHz) to zigzag (for the letter 'L' image, 14.8-15.2 GHz) [13].

Terahertz (0.1-10 THz) wireless communication is a cornerstone of the next 6G wireless. THz frequencies have the potential to dramatically increase wireless capacity performance and enable high-resolution environment sensing. THz waves can penetrate substances that are opaque to visible and infrared light and possess higher spatial resolution, penetration depth, and non-ionization safety. However, the research on THz metasurface holography images is still in its nascent stages. Reference [14] reported single-pixel THz near-field imaging, achieving $\lambda_0/45$ resolution at 0.75 THz and $\lambda_0/133$ resolution at 0.5 THz. In reference [15], single-pixel computational ghost imaging with reflective multilayer metasurface holography was introduced in an optical encryption scheme. A reconfigurable and multifunctional 3-bit coding reflection single layer metasurface at 0.95 THz is proposed by integrating photosensitive Ge material into the metasurface unit, and switching between vortex beams and holographic imaging was achieved under the RCP incidence by optically controlling [16]. A multilayer metasurface achieved reconfigurable multichannel holographic imaging in the THz band by integrating vanadium dioxide (VO_2) into the metasurface unit [17]. Holographic letters 'R' and 'L' were achieved when temperature is above 68 °C, and holographic numbers '2' and '6' were generated in other two channels when temperature is below 68 °C.

Graphene has garnered extensive research attention due to its mechanical robustness, outstanding thermal stability, and chemical and biological stability. Reconfigurable multi-channel reflected light beams were obtained by integrating graphene into the metasurface unit cell [18]. A multifocal graphene orbital angular momentum (OAM) metalen was designed by using spatially multiplexed single-focus with different focal lengths and topological charges [19].

As mentioned above, multi-channel holographic multiplexing images have been realized using transmission, reflection, or transmission-reflection mode metasurface. Full-space meta-holograms offer the advantages of miniaturization and high integration. However, to the knowledge of the authors, the above full space metasurface is realized by controlling orthogonal linearly polarized waves, and there is no dynamic modulation of dual modes (transmission and reflection) based on phase change material. In THz frequency band, there is no reflection-transmission dual mode metasurface for holographic imaging, and there is no dynamic modulation holographic imaging based on graphene. Here, reflection-transmission dynamic modulation THz single-layer propagation-geometric phase dielectric metasurface is proposed based on graphene. The reflection and transmission modes can be switched by controlling the Fermi energy level of graphene integrated into the metasurface unit. In the meantime, the metasurface is also reconfigurable in reflection or transmission mode by switching the feed polarization among RCP, LCP and LP. As example, a reflection and transmission propagation-geometric phase metasurface is designed, and reconfigurability between reflection and transmission modes is achieved by switching the graphene Fermi energy level between 0.1 eV and 0.9 eV. The operation bandwidth for reflection mode is from 1.15 THz to 1.35 THz (16%), and from 1.32 THz to 1.6 THz (19%) for transmission mode. High holographic efficiencies (42.5% to 49%), and six-channel holographic imaging are obtained.

 doi:10.20944/preprints202407.2254.v1

2. Materials and Methods

Figure 1 shows the schematic diagram for the dual mode reconfigurable multifunctional metasurface, which consists of three layers: indium telluride pillar unit layer (top), F4B substrate (middle), and graphene layer (bottom). Figure 1 shows the reconfigurable holographic imaging obtained by switching the incidence polarization in reflection and transmission modes, respectively. Figure 1c is the phase switching sketch map: metal when E_f = 0.9eV, insulator when E_f = 0.1eV. The proposed metasurface works in reflection and transmission modes when E_f =0.9eV and 0.1eV, respectively. The reconfiguration among the Chinese characters '华', '工' and '华 工'are achieved by switching LCP, RCP and LP incidence, respectively. The operation frequency range is 1.15THz – 1.35THz (16%) for reflection mode, and 1.32 THz - 1.6 THz (19%) for transmission mode. The holographic imaging is co- and cross- polarization for reflection and transmission modes, respectively.

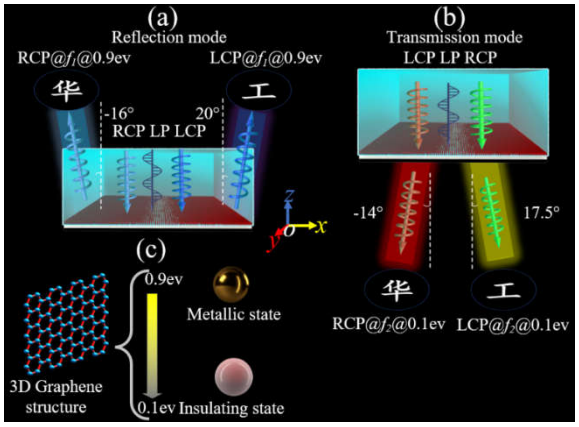

Figure 1. Schematic diagram for the dual-mode reconfigurable multifunctional metasurface. (**a**) Reconfigurable reflection mode. (**b**) Reconfigurable transmission mode. (**c**) Graphene switching sketch map: metal when E_f = 0.9 eV, insulator when E_f = 0.1eV.

2.1. Phase Change Principle of Graphene

The electric conductivity of graphene is the sum of inter-band and intra-band conductivity according to the Kubo equation. The inter-band conductivity can be neglected at room temperature in the lower THz frequency band, and the surface electric conductivity $\sigma_g(\omega)$ of graphene is described as follows [20].

$$\sigma_g(\omega) \approx \sigma_{\text{intra}}(\omega) = j\frac{e^2 K_B T}{\pi\hbar^2(\omega + j\tau^{-1})}\left(\frac{E_f}{K_B T} + 2In\left(exp\left(-\frac{E_f}{K_B T}\right)+1\right)\right) \quad (1)$$

where ω, e, K_B, T, $\hbar$, τ and E_f are the angular frequency, electron charge, Boltzmann constant, environmental temperature, Planck's constant, the relaxation time and the Fermi energy level, respectively. The conductivity of graphene can be continuously tuned by manipulating its Fermi energy via extra voltage. Graphene functions as the dielectric when E_f = 0.1 eV, and is in metallic state when E_f = 0.9 eV [21]. Here, set τ = 1 *ps* and T = 300 *K*. The conductivity of graphene is a function of ω and E_f according to Equation (1). In this paper, the proposed reconfigurable metasurface works in transmission mode at frequency f_1 when E_f = 0.1 eV, and in reflection mode at frequency f_2 when E_f = 0.9 eV. The metallic 2D graphene layer acts as ground plane in reflection mode.

2.2. The Phases (ϕ_x, ϕ_y, β) Calculation Principle for Geometry-Propagation Phase Unit

After the phase distribution map for the metasurface is calculated according to GS algorithm, a unit with phase (ϕ_x, ϕ_y, β) are designed to implement the calculated phase distribution map. The physical model of the unit phase (ϕ_x, ϕ_y, β) vs the outgoing wave phase is as follows.

When a unit with x-axis or y-axis symmetry is rotated an angle β in the xoy plane, and a propagation-geometric phase metasurface unit is formed.

 doi:10.20944/preprints202407.2254.v1

For transmission metasurface, assume the transmission amplitude $t_{x(y)}$ for *x*- or *y*- polarization approaches 1. When the transmission metasurface is excited by the normal CP incidence plane wave, the co-polarized (J_{co}) and cross-polarized (J_{cross}) components are given by [19]:

$$\begin{cases} J_{co} = \frac{1}{2}\left(e^{i\phi_x} + e^{i\phi_y}\right) = \cos\frac{\phi_x - \phi_y}{2} \times e^{i\frac{(\phi_x+\phi_y)}{2}} \\ J_{cross} = \frac{1}{2}\left(e^{i\phi_x} - e^{i\phi_y}\right) \times \left(e^{i2\beta} \bullet \hat{\sigma}_R + e^{-i2\beta} \bullet \hat{\sigma}_L\right) \\ \quad = \sin\frac{\phi_x - \phi_y}{2} \times e^{i\frac{(\phi_x+\phi_y+\pi)}{2}} \times \left(e^{i2\beta} \bullet \hat{\sigma}_R + e^{-i2\beta} \bullet \hat{\sigma}_L\right) \end{cases} \quad (2)$$

where $\hat{\sigma}_R = \frac{1}{2}\begin{bmatrix} 1 & -i \\ -i & -1 \end{bmatrix}$ and $\hat{\sigma}_L = \frac{1}{2}\begin{bmatrix} 1 & i \\ i & -1 \end{bmatrix}$ are defined as polarization operators and the subscripts L and R represent LCP and RCP, respectively. ϕ_x and ϕ_y are the propagation phases for x and y polarization, respectively. β is the rotated angle in the *xoy* plane. From Equation (2), the amplitude (t) and phase (ϕ) for J_{co} and J_{cross} are as follows:

$$\begin{cases} t_{co} = \cos(\phi_x - \phi_y)/2 \\ t_{cross} = \sin(\phi_x - \phi_y)/2 \end{cases} \quad (3)$$

$$\begin{cases} \phi_{co} = (\phi_x + \phi_y)/2 \\ \phi_{cross} = (\phi_x + \phi_y + \pi)/2 \pm 2\beta \end{cases} \quad (4)$$

From Equation (4), the phase for the cross-dual CP can be independently controlled as follows: $\phi_{crossRCP} = (\phi_x + \phi_y + \pi)/2 + 2\beta$ for RCP, $\phi_{crossLCP} = (\phi_x + \phi_y + \pi)/2 - 2\beta$ for LCP. If $\phi_x = \phi_y + \pi$, the co-polarized component is suppressed according to Equation (2), and the metasurface convert RCP (LCP) incident wave to outgoing LCP (RCP) wave. Then the propagation phase and rotation angle of the unit can be derived as by Equation (4):

$$\begin{cases} \phi_x = \phi_y + \pi \\ \phi_y = (\phi_{crossRCP} + \phi_{crossLCP} - 2\pi)/4 \\ \beta = (\phi_{crossRCP} - \phi_{crossLCP})/4 \end{cases} \quad (5)$$

For reflection metasurface. Assume the reflection amplitudes for *x*- or *y*- polarization keeps as unity ($r_x = r_y = 1$), and ($\phi_x - \phi_y = \pi$). When the reflection metasurface is excited by a normal CP incidence plane wave, the Jones matrix of the outgoing wave is as follows: [23,24]:

$$\begin{bmatrix} E_{LL}^r \\ E_{RR}^r \end{bmatrix} = C'MJM^{-1}C^{-1} = \begin{pmatrix} e^{(\phi_x - i2\beta)} & 0 \\ 0 & e^{(\phi_x + i2\beta)} \end{pmatrix} \begin{bmatrix} E_L^i \\ E_R^i \end{bmatrix} \quad (6)$$

where E_L^i, E_{LL}^r, E_{LL}^r and E_{RR}^r are represent the incident LCP wave, incident RCP wave, LCP outgoing wave, and RCP outgoing wave, respectively. $\boldsymbol{M} = \begin{bmatrix} \boldsymbol{\cos\beta} & \boldsymbol{-\sin\beta} \\ \boldsymbol{\sin\beta} & \boldsymbol{\cos\beta} \end{bmatrix}$, $J = \begin{bmatrix} e^{j\phi_x} & 0 \\ 0 & e^{j\phi_y} \end{bmatrix}$, $C = \frac{1}{2}\begin{bmatrix} 1 & i \\ 1 & -i \end{bmatrix}$ and $C' = \frac{1}{2}\begin{bmatrix} 1 & -i \\ 1 & i \end{bmatrix}$. The cross-polarized component is suppressed, and the outgoing wave is co-polarized. The co-polarization phases for LCP and RCP waves are as follows:

$$\begin{cases} \phi_{co-LCP} = \phi_x - 2\beta \\ \phi_{co-RCP} = \phi_x + 2\beta \end{cases} \quad (7)$$

2.3. Gerchberg-Saxton (GS) Algorithm

The Gerchberg-Saxton (GS) algorithm, which was originally proposed by D. Gerchberg and W. Saxton in 1972 [22], is an iterative algorithm commonly used in phase retrieval for holographic imaging based on Fourier transform and inverse Fourier transform. The iteration starts from the measured amplitude information of the input image, and ends until the error threshold $(|E_i| - |E_0|) < \varepsilon$ is met. Here GS algorithm is used to obtain the phase distribution map of the phase gradient metasurface, and the basic steps and method are shown in Figure 2.

 doi:10.20944/preprints202407.2254.v1

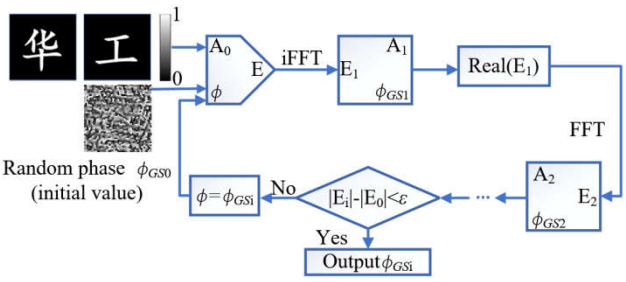

Figure 2. Basic flowchart of the GS algorithm.

The required images '华', '工' in z axis direction are established by Computer holography technology based on MATLAB. First, painting software is used to draw the required images (including the black background and the white images). Second, the amplitude matrix A_0 (m×n) in the image area is obtained by MATLAB function 'imread' and 'binary'. In A_0 (m×n), the intensities are "1" and "0" for points (x, y, 0) in white and black, respectively. Third, the MATLAB function 'random' generates a random phase matrix Φ_{GS0} (m×n). Apply Fourier transform to the matrices A_0 and Φ_{GS0}, and obtain amplitude and phase matrices in frequency domain A_1 and Φ_{GS1}. Then, update all the amplitude matrix values in A_1 (m×n) into 1, that is, $A'_1(x, y) = 1$. Perform inverse Fourier transform to A'_1 and Φ_{GS1}, and obtain amplitude and phase matrices in time domain A_2 and Φ_{GS2}. Repeat iterative operations of step 2 and step 3, and update the i-th iteration amplitude $A_i(x, y)$ to $A'_i(x, y) = 1$ until the error threshold $(|E_i| - |E_0|) < \varepsilon$, where $E = A\exp(i\phi_{GS})$. Then the phase distribution map for the Metasurface is obtained.

2.4. The Total Compensated Phase Calculation Based on Transmission Mode

The metasurface is designed in transmission mode at f_1 when $E_f = 0.1$ eV. Under LCP incidence, a holographic imaging RCP '华' is generated in direction (θ_1, 0°). Under RCP incidence, a holographic imaging LCP '工' is generated in direction (θ_2, 0°). The phase compensation for the metasurface obtained by GS algorithm is Φ_{GS}, which is for the images in normal direction. An additional compensated phase is added for the desired imaging direction (θ, 0°), and the compensated phase for RCP '华' or LCP '工' for the metasurface unit located at (x, y, 0) is as follows:

$$\begin{cases} \phi_{cross-RCP华} = \phi_{华} + \dfrac{2\pi f_1}{c} \times (\sin\theta_1) \times x \\ \phi_{cross-LCP工} = \phi_{工} + \dfrac{2\pi f_1}{c} \times (\sin\theta_2) \times x \end{cases} \tag{8}$$

Then the compensated phase parameters (ϕ_x, ϕ_y, β) of the metasurface unit for reconfigurable multifunctional holographic imaging for '华', '工' and '华工' is calculated by Equation (5) and Equation (8).

2.5. The Imaging Direction Deduction for Reflection Mode

By switching the bottom graphene layer from insulator to metal states, the metasurface designed in transmission mode can be made to work in reflection mode with the bottom graphene layer acting as a ground plane. According to Equation (6), the holographic imaging of (RCP, '华', θ_1, 0°) and (LCP, '工', θ_2, 0°) designed in transmission mode has changed into co-polarized imaging of (LCP, '工', θ_3, 0°) and (RCP, '华', θ_4, 0°) in reflection mode as shown in Figure 3. Though the phase distribution map of the metasurface is calculated based on transmission mode, (LCP, '工', θ_3, 0°) and (RCP, '华', θ_4, 0°) are generated under LCP and RCP incidences in reflection mode, respectively. Because the graphene permittivity is a function of its state, the operation frequency f_2 and direction $\theta_{3(4)}$ for reflection mode are different from f_1 and $\theta_{1(2)}$ in transmission mode. The direction $\theta_{3(4)}$ is calculated as follows:

Preprints.org (www.preprints.org) | NOT PEER-REVIEWED | Posted: 29 July 2024 doi:10.20944/preprints202407.2254.v1

$$\begin{cases} \phi_{cross-RCP华} = \phi_{co-RCP华} = \phi_{华} + \dfrac{2\pi f_2}{c} \times (\sin\theta_4) \times x \quad (under\ LCP\ incidence) \\ \phi_{cross-LCP工} = \phi_{co-LCP工} = \phi_{工} + \dfrac{2\pi f_2}{c} \times (\sin\theta_3) \times x \quad (under\ RCP\ incidence) \end{cases} \tag{9}$$

From Equations (8) and (9), θ_3 and θ_4 are deduced as follows.

$$\begin{cases} \theta_3 = \arcsin\left(\dfrac{f_1}{f_2}\sin(\theta_2)\right) \\ \theta_4 = \arcsin\left(\dfrac{f_1}{f_2}\sin(\theta_1)\right) \end{cases} \tag{10}$$

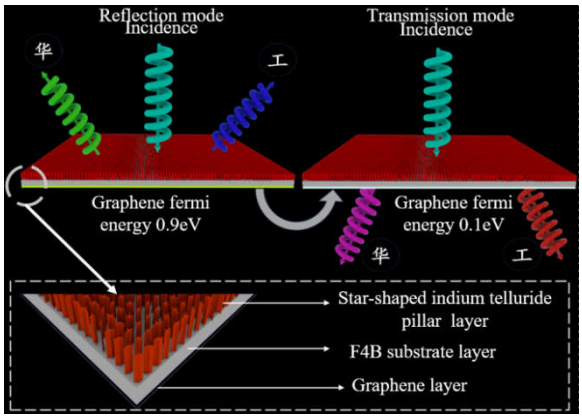

Figure 3. The transmission-reflection reconfigurable metasurface.

In summary, based on the above analysis, the proposed metasurface can be switched between transmission and reflection modes, and the holographic imaging can be reconfigured by switching the incident polarization when operating in transmission or reflection mode. Six holographic imaging channels are achieved, as shown in Table 1.

Table 1. Six holographic imaging channels of proposed metasurface.

Incidence	Fermi Energy	Frequency	Channel	Hologram (Polarization, Pattern, Reflection angle)
LCP	0.1 eV	f1	T1 [1]	RCP, '华', (θ1,0°)
	0.9 eV	f2	R1	LCP, '工', (θ3,0°)
RCP	0.1 eV	f1	T2	LCP, '工', (θ2,0°)
	0.9 eV	f2	R2	RCP, '华', (θ4,0°)
LP	0.1 eV	f1	T3	RCP, '华', (θ1,0°), and LCP, '工', (θ2,0°)
	0.9 eV	f2	R3	RCP, '华', (θ4,0°), and LCP, '工', (θ3,0°),

[1] (T~ = Transmission channel ~, Rx = Reflection channel ~).

2.6. Unit Cell Design

The proposed dual-mode metasurface is excited by normal plane wave as in Figures 1 and 3. Open boundaries were set as boundary conditions. As example, dual-mode reconfigurable multifunctional holographic imaging are designed in order to validate the above design method: (1) Reconfigurable Chinese characters with cross-polarized in transmission mode are achieved when E_f = 0.1 eV: (a) (RCP, '华', -14°, 0°), (b) (LCP, '工', 17.5°, 0°), and (c) both (RCP, '华', -14°, 0°) and (LCP, '工', 17.5°, 0°) by switching LCP, RCP and LP incidence, respectively. (2) Reconfigurable multifunctional holographic imaging (Chinese characters) with co-polarized are achieved in

Preprints.org (www.preprints.org) | NOT PEER-REVIEWED | Posted: 29 July 2024 doi:10.20944/preprints202407.2254.v1

reflection mode when E_f = 0.9 eV: (a) (RCP, '华', -16°, 0°), (b) (LCP, '工', 20°, 0°), (c) both (RCP, '华', -16°, 0°) and (LCP, '工', 20°, 0°) by switching the RCP, LCP and LP incidence, respectively. All the curves and field patterns are simulated by CST Microwave Studio software.

To realize the designed dual-mode reconfigurable multifunctional holographic imaging, a unit cell is proposed to implement the phase (ϕ_x, ϕ_y, β) at (x, y, 0) calculated by Equation (5), which is shown in Figure 4. Figure 4a–c show the simulation Floquet model, top and side views for the unit, respectively, which consists of a star-shaped indium telluride pillar (ε_r =19, tan δ = 0.001) in the top and a 2D bottom graphene layer separated by an F4B substrate with a dielectric constant 2.2, tan δ = 0.003. All geometry parameters are marked in Figure 4, and the optimized parameters are as follows: p = 123 μm, w = 11 μm, h_1 = 150 μm, h_2 = 0.5 μm and h_3 = 0.05 μm. The propagation phases ϕ_x and ϕ_y are controlled by l_x and l_y, respectively, and the geometry phase is controlled by rotating the unit cell counter clockwise β degree.

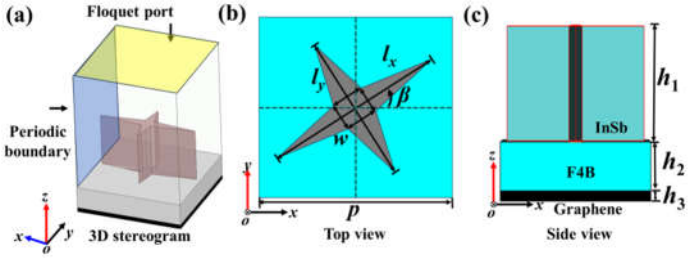

Figure 4. The proposed unit cell: (**a**) 3D stereogram, (**b**) Top view, (**c**) Side view.

Under normal x- (y-) polarized incident excitation: (1) For reflection mode at 1.31THz, 1.325THz and 1.336THz, Figure 5a shows the simulated S_{11} and phase $\phi_{x(y)}$ as a function of $l_{x(y)}$, and Figure 5b shows the simulated S_{11} and phase $\phi_{y(x)}$ as a function of $l_x(_y)$. (2) For transmission mode at 1.455THz, 1.465THz, and 1.473 THz: Figure 5c shows the simulated amplitude (S_{21}) and phase $\phi_{x(y)}$ curves as function of $l_{x(y)}$, and Figure 5d is the simulated amplitude (S_{21}) and phase $\phi_{y(x)}$ curves as function of $l_{x(y)}$. For both transmission and reflection modes when $l_{x(y)}$ varies from 15 μm to 113 μm: (1) The phase of the co-polarization $\phi_{x(y)}$ increases from -450° to -90°, covering a 360° phase range. (2) The phase shift of the cross-polarization $\phi_{y(x)}$ remains basically unchanged, indicating that ϕ_x and ϕ_y can be independently adjusted by l_x and l_y, respectively. S_{11} > 0.99 for reflection mode, and S_{21} > 0.85 for transmission mode. The phase $\phi_{x(y)}$ curves versus $l_x(_y)$ for different frequency points (at 1.31THz, 1.325THz for reflection mode or at 1.455 THz, 1.465 THz, and 1.473 THz for transmission mode) are parallel, indicating that the metasurface can operate within a certain bandwidth. According to Figure 5a,c, a polynomial formula for the relationship between $\phi_x(_y)$ and $l_x(_y)$ can be fitted as follows:

$$\begin{aligned}\phi_{x(y)} &= 392.7\times\sin(0.027\times l_{x(y)}+0.2954)+264.3\times\sin(0.075\times l_{x(y)}+0.1413)\\ &\quad +209.3\times\sin(0.08\times l_{x(y)}+2.699)\end{aligned} \tag{11}$$

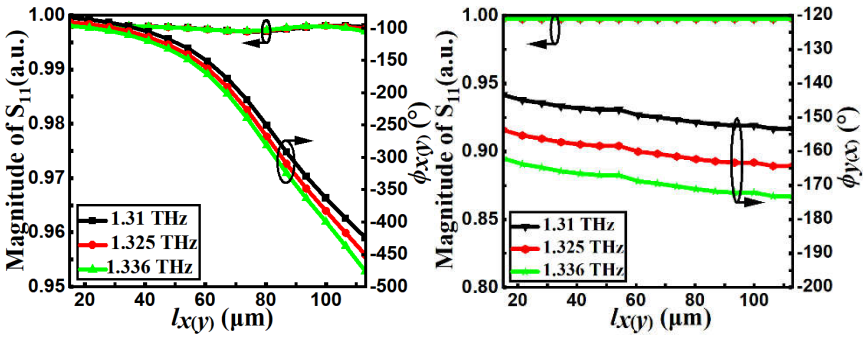

Preprints.org (www.preprints.org) | NOT PEER-REVIEWED | Posted: 29 July 2024 doi:10.20944/preprints202407.2254.v1

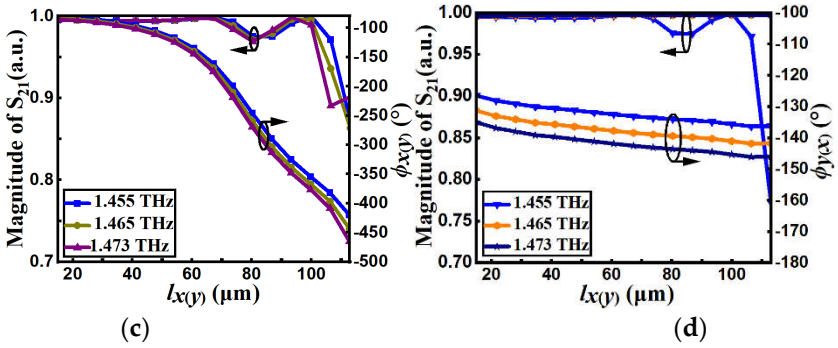

Figure 5. (**a**) Simulated S_{11} and phase shift $\phi_x(y)$ as a function of $l_x(y)$ at 1.31, 1.325, and 1.336 THz. (**b**) Simulated S_{11} and phase shift $\phi_y(x)$ as a function of $l_x(y)$ at 1.31, 1.325, and 1.336 THz. (**c**) Simulated S_{21} and phase shift $\phi_x(y)$ as a function of $l_x(y)$ at 1.455, 1.465, and 1.473 THz. (**d**) Simulated S_{21} and phase shift $\phi_y(x)$ as a function of $l_x(y)$ at 1.455, 1.465, and 1.473 THz.

When l_x =15 μm, Figure 6 shows the curves of the geometric phase as a function of the rotation angle β for reflection mode when l_x=15um (at 1.31THz, 1.325THz, and 1.336 THz) and transmission mode (at 1.455THz, 1.465THz, and 1.473THz). When β ranges from 0° to 180°, the geometric phase shift covers 360°, and the geometric phase vs β curves at different frequency points (1.31THz, 1.325THz and 1.336THz for reflection mode or 1.455THz, 1.465THz, and 1.473 THz for transmission mode) are parallel.

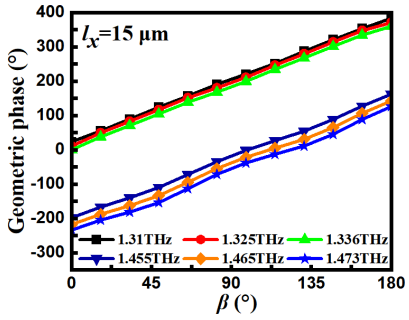

Figure 6. Simulated geometric phase versus β curves when l_x = 15 μm.

2.7. Metasurface Design

The transmission-reflection reconfigurable metasurface shown in Figure 3 is formed by the proposed 91×91 unit cells with size 11.193mm×11.193mm×0.15mm ($50.4\lambda_0 \times 50.4\lambda_0 \times 0.68\lambda_0$) for dual-mode reconfigurable multifunctional holographic imaging: (1) Reconfigurable cross-polarized holographic imaging in transmission mode when E_f = 0.1eV: (a) (RCP, '华', -14°, 0°), (b) (LCP, '工', 17.5°, 0°), and (c) both (RCP, '华', -14°, 0°) and (LCP, '工', 17.5°, 0°) by switching LCP, RCP and LP incidence, respectively. (2) Reconfigurable multifunctional co-polarized holographic imaging in reflection mode when E_f = 0.9eV: (a) (RCP, '华', -16°, 0°), (b) (LCP, '工', 20°, 0°), (c) both (RCP, '华', -16°, 0°) and (LCP, '工', 20°, 0°) by switching the RCP, LCP and LP incidence, respectively.

The compensated phase distributions for ϕ_x, ϕ_y and 2β according to Equation (5) are shown in Figure 7, and then the corresponding geometry length distributions for l_x, l_y in the metasurface are obtained according to Equation (11).

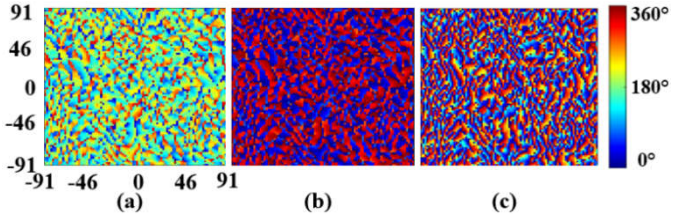

Figure 7. Phase distribution for the designed metasurface: (a) Propagation phase ϕ_x. (b) Propagation phase ϕ_y. (c) Geometric phase 2β.

 doi:10.20944/preprints202407.2254.v1

3. Results

3.1. 2D and 3D Far-Field Properties

The far-field radiation patterns at 1.325 THz or 1.465 THz under LCP, RCP and LP incidence are shown in Figure 8. Figure 8a,b show the three dimension (3D) and 2D far-field radiation patterns for reflection and transmission modes, respectively. Reconfigurable cross-polarized holographic imaging is achieved at 1.465 THz in transmission mode among ('华', RCP, θ = -14°, φ = 0°), ('工', LCP, θ = 17.5°, φ = 0°) and both ('华', RCP, θ = -14°, φ = 0°) and ('工', LCP, θ = 17.5°, φ = 0°) by switching LCP, RCP and LP incidence, respectively. Reconfigurable multifunctional co-polarized holographic imaging is achieved at 1.325 THz in reflection mode among ('华', RCP, θ = -16°, φ = 0°), '工', LCP, θ = 20°, φ = 0°), and both ('华', RCP, θ = -16°, φ = 0°) and ('工', LCP, θ = 20°, φ = 0°) by switching the RCP, LCP and LP incidence, respectively. The simulated and calculated holographic imaging are in good agreement. Because LP wave can be decomposed into two equal LCP and RCP waves, both the LCP and RCP excitation are done simultaneously, and the holographic imaging for LP incidence are the holographic imaging sum of LCP and RCP incidences.

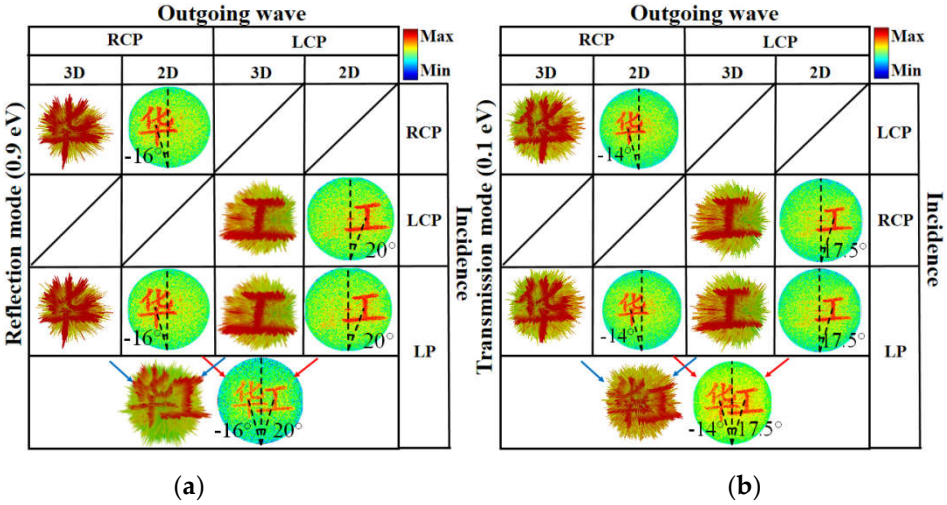

(**a**) (**b**)

Figure 8. Simulated 3D and 2D far-field holographic imaging under RCP, LCP and LP incidence: for reflection mode at (**a**), for transmission mode (**b**).

3.2. Analysis of the Bandwidth Characteristics

The simulated 3D and 2D far-field holographic imaging with co-polarization under RCP and LCP incidences in reflection mode at 1.15THz, 1.25THz and 1.35THz are shown in Figure 9a. The profile remains unchanged across different frequencies, indicating an operation bandwidth from 1.15THz to 1.35THz (16%). Figure 9b illustrates the simulated 3D and 2D far-field holographic imaging with cross-polarization under RCP and LCP incidences in transmission mode at 1.32THz, 1.465THz and 1.6THz. The profile remains nearly unchanged across different frequencies, indicating an operation bandwidth from 1.32THz to 1.6THz (19%).

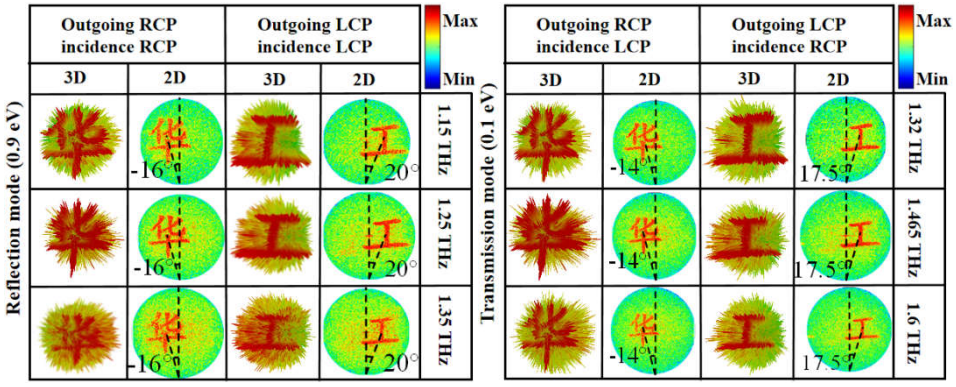

 doi:10.20944/preprints202407.2254.v1

(**a**) (**b**)

Figure 9. Simulated 3D and 2D far-field holographic imaging under RCP and LCP incidence: (**a**) co-polarization in reflection mode at 1.15 THz, 1.25 THz and 1.35 THz, (**b**) cross- polarization in transmission mode at 1.32 THz, 1.465 THz and 1.6 THz.

3.3. Holographic Efficiencies

To evaluate the imaging quality of the designed metasurface, we calculated the holographic efficiency for both transmission and reflection modes as shown in Figure 8. The calculation formula for holographic efficiency is referenced in reference [17,25].

$$\eta = \frac{\int_0^{2\pi}\int_0^{\pi}|E_r(\theta,\varphi)|^2 \sin\theta d\theta d\varphi}{\int_0^{2\pi}\int_0^{\pi}|E_m(\theta,\varphi)|^2 \sin\theta d\theta d\varphi} \quad (12)$$

where η represents the holographic efficiency, E_r (θ, φ) and E_m (θ, φ) are the far-field scattering patterns from the metasurface and the corresponding metal mirror with the same size, respectively. Figure 10a,b are the holographic efficiencies under LCP, RCP, and LP excitation for reflection and transmission modes, respectively. The holographic efficiencies for the reflection mode at 1.25 THz under LCP, RCP, and LP incidences are 42.5%, 42.8%, and 49%, respectively. The holographic efficiency for the transmission mode at 1.465THz are 44.8%, 45.1%, and 47% for LCP, RCP, and LP incidences, respectively.

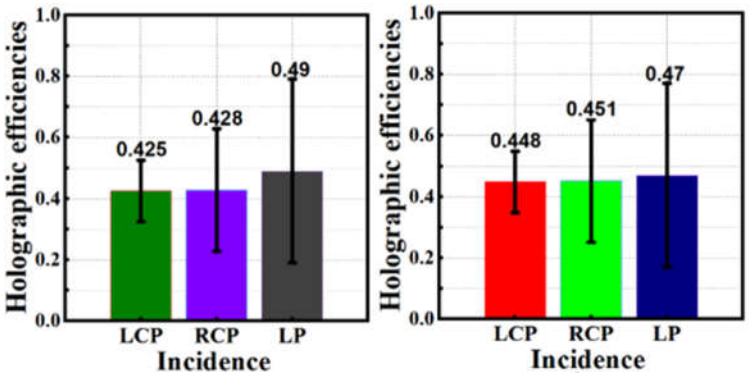

(**a**) (**b**)

Figure 10. Holographic efficiencies under LCP, RCP, and LP incidences: (**a**) for reflection mode at 1.25 THz, (**b**) for transmission mode at 1.465 THz.

4. Discussion

A comparison in operation frequency, holographic imaging channel number, operation mode number, operation bandwidth and holographic efficiency has been made between the proposed design and published holographic metasurfaces as in Table 2. References [9–11,17] only work in only reflection or transmission mode. Ours works in both reflection and transmission modes, and is reconfigurable for reflection or transmission mode by switching among the RCP, LCP and LP incidence. In addition, ours has more holographic imaging channel numbers and higher holographic efficiency.

Table 2. Comparison of the proposed metasurface and published holographic metasurfaces.

Reference	Frequency	Number of channels	TS or RS	Relative bandwidth	Holographic efficiency
[9]	375 THz	2	TS	0	NA[1]
[10]	7.5, 13 GHz	4	RS	0	NA

 doi:10.20944/preprints202407.2254.v1

[11]	7.2, 9.1, 10.9, 15.2 GHz	4	TS	0	NA
[17]	1.1-1.6 THz	4	RS	37%	44.2%, 45.9%
This work	1.15-1.35, 1.32-1.6 THz	6	TS, RS	16%(TS)，19% (RS)	42.5%，42.8%，49% (TS), 44.8%，45.1%，47% (RS)

1 (NA = Not Available, TS = Transmission State, RS = Reflection State).

In addition, we also discuss the fabrication of the proposed metasurface. While our design theory has been validated from a simulation perspective, we still face two key challenges. The first challenge pertains to the fabrication of metasurface. Figure 11 illustrates potential fabrication methods. Firstly, the F4B material layer can be obtained through self-assembly to form the required dielectric substrate. Secondly, there are two methods to obtain the top layer of indium telluride. One approach involves chemical vapor deposition (CVD), whereby indium telluride thin films are deposited on the F4B substrate, with control over temperature, humidity, and deposition rate to achieve the desired material thickness and quality. Another method entails utilizing physical vapor deposition (PVD), employing techniques such as sputtering or evaporation to deposit indium telluride material on the substrate, with deposition parameters controlled to achieve the desired dielectric dimensions. Finally, the bottom graphene layer can be prepared through mechanical exfoliation, as referenced in reference [26], for transferring graphene onto the substrate. Alternatively, graphene can be grown directly on the F4B material bottom using CVD, with precise management of reaction conditions to achieve the required graphene thickness.

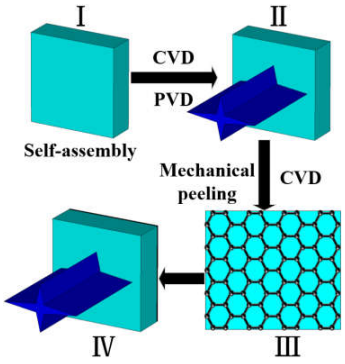

Figure 11. Fabrication chart of the proposed metasurface.

The second challenge pertains to the method of controlling graphene's chemical potential. As documented in reference [18,20,21,27], the application of an electric field between the graphene layer and the upper dielectric can effectively manipulate the carrier concentration of graphene, subsequently allowing for the adjustment of the Fermi level. Moreover, techniques such as chemical doping, direct laser writing, the imposition of mechanical strain, and the utilization of piezoelectric effects can be employed to modulate the lattice structure of graphene. This, in turn, alters its electronic properties and facilitates the subsequent adjustment of the Fermi level positioning.

5. Conclusions

This paper develops a multifunctional and reconfigurable reflection-transmission dual-mode THz dielectric holographic metasurface formed by propagation - geometry composite units. The dual-mode is achieved by controlling the Fermi energy level of graphene integrated into the metasurface unit, and the proposed metasurface works in reflection and transmission modes when E_f = 0.9 eV, 0.1eV, respectively. The reconfigurability is realized by switching incidence polarization. The metasurface is designed based on transmission mode, and the physical model switching to the

 doi:10.20944/preprints202407.2254.v1

reflection mode is established. For the first time, dynamic modulation reflection-transmission holographic imaging metasurface based on graphene is developed. As example, a multifunctional and reconfigurable metasurface has been developed: (1) Reconfigurable cross-polarized three-channel holographic imaging in transmission mode from 1.32THz to 1.6THz: ('华', RCP, θ = -14°, φ = 0°), ('工', LCP, θ = 17.5°, φ = 0°) and ('华', RCP, θ = -14°, φ = 0° and '工', LCP, θ = 17.5°, φ = 0°) by switching LCP, RCP and LP incidence, respectively. (2) Reconfigurable co-polarized three-channel holographic imaging in reflection mode from 1.15THz to 1.35THz: ('华', RCP, θ = -16°, φ=0°), ('工', LCP, θ = 20°, φ = 0°), and ('华', RCP, θ = -16°, φ = 0° and '工', LCP, θ = 20°, φ = 0°) by switching the RCP, LCP and LP incidences, respectively. Compare with published holographic imaging, ours has more channel numbers (six holographic imaging channels) and higher holographic efficiency (42.5% to 49%). These characteristics make the proposed metasurface has potential applications in information encryption transmission, multi-channel imaging, and other related fields.

Author Contributions: Conceptualization, H.H. and J.W.; methodology, J.W.; software, J.W.; validation, H.H. and J.W.; formal analysis, J.W.; investigation, J.W.; resources, J.W.; data curation, J.W.; writing—original draft preparation, J.W.; writing—review and editing, H.H.; visualization, J.W.; supervision, H.H. and J.W. All authors have read and agreed to the published version of the manuscript.

Funding: This research was funded by the Guangdong Major Project of Basic and Applied Basic Research (No.2023B0303000008), the National Key Research and Development Program of China (No.2020YFB1807300) and State Key Laboratory of Radio Frequency Heterogeneous Integration (Shenzhen University), (No.202306).

Data Availability Statement: The original contributions presented in the study are included in the article, further inquiries can be directed to the corresponding authors.

Acknowledgments: The valuable comments of the reviewers and associate editor are gratefully appreciated.

Conflicts of Interest: The authors declare no conflicts of interest.

References

1. Tian, Y.; Wei, Q.; Cheng, Y.; Liu, X. Acoustic holography based on composite metasurface with decoupled modulation of phase and amplitude. *Applied Physics Letters* **2017**, *110*, 19190.
2. Xie, Y.; Shen, C.; Wang, W. et al. Acoustic holographic rendering with two-dimensional metamaterial-based passive phased array. *Sci Rep* **2016**, *6*, 35437.
3. Chen, W.; Javidi, B.; Chen, X. Advances in optical security systems. *Adv. Opt. Photon.* **2014**, *6*, 120–155.
4. Jiang, Q.; Jin, G.; Cao, L. When metasurface meets hologram: principle and advances. *Adv. Opt. Photon.* **2019**, *11*, 518–576.
5. Huang, L., Chen, X., Mühlenbernd, H. et al. Three-dimensional optical holography using a plasmonic metasurface. *Nat Commun* **2013**, *4*, 2808.
6. Li, Z., Dai, Q., Mehmood, M.Q. et al. Full-space cloud of random points with a scrambling metasurface. *Light Sci Appl* **2018**, *7*, 63.
7. Deng, L., Deng, J., Guan, Z. et al. Malus-metasurface-assisted polarization multiplexing. *Light Sci Appl* **2020**, *9*, 101.
8. Li, Z.; Chen, C.; Guan, Z.; Tao, J.; Chang, S.; Dai, Q.; Xiao, Y.; Cui, Y.; Wang, Y.; Yu, S.; et al. Three-Channel Metasurfaces for Simultaneous Meta-Holography and Meta-Nanoprinting: A Single-Cell Design Approach. *Laser & Photonics Reviews* **2020**, *14*, 200003.
9. Wang, H.; Zhang, B.; Han, C.; Ding, J. Polarization-multiplexed wavefront-engineering by all-dielectric metasurface with asymmetric polarization-decoupled meta-atoms. *Opt. Express* **2021**, *29*, 32377–32387.
10. Zhang, Q.; Wang, J.; Xie, R.; Gu, Z.; Zhang, Z.; Wang, X.; Zhang, H.; Chen, C.; Chen, W.; Ding, J.; et al. Four-channel joint- polarization-frequency-multiplexing encryption meta-hologram based on dual-band polarization multiplexing meta-atoms. *Opt. Express* **2023**, *31*, 17569–17579.
11. Zhu, L.; Wei, J.; Dong, L.; Shang, G.; Guan, C.; Burokur, S.N.; Ding, X. Four-channel meta-hologram enabled by a frequency-multiplexed mono-layered geometric phase metasurface. *Opt. Express* **2024**, *32*, 4553–4563.
12. Zhu, L.; Zhou, W.; Dong, L.; Guan, C.; Shang, G.; Ding, X.; Burokur, S.N.; Wu, Q. Full Space Control of Meta-Holograms Utilizing a Bilayered Patterned Coding Metasurface. *IEEE Antennas and Wireless Propagation Letters* **2022**, *21*, 322–326.
13. Wang, K.; Liao, D.; Wang, H. Reconfigurable origami hologram based on deep neural networks. *Opt. Lett.* **2024**, *49*, 2041–2044.
14. Chen, S.C.; Du, L.H.; Meng, K.; Li, J.; Zhai, Z.H.; Shi, Q.W.; Li, Z.R.; Zhu, L.G. Terahertz wave near-field compressive imaging with a spatial resolution of over λ/100. *Opt. Lett.* **2019**, *44*, 21–24.

15. Liu, H.C.; Yang, B.; Guo, Q.; Shi, J.; Guan, C.; Zheng, G.; Mühlenbernd, H.; Li, G.; Zentgraf, T.; Zhang, S. Single-pixel computational ghost imaging with helicity-dependent metasurface hologram. *Science Advances* **2017**, *3*, e1701477.
16. Dai, Y.; Chen, C.; Gao, P.; Lu, X.; Zhao, J.; Wan, Y.; Wang, X.; Zhao, S.; Liu, H. 3-bit reconfigurable THz metasurface based on structured light illumination for vortex beams and holographic imaging. *Optics Laser Technology* **2024**, *169*, 109951.
17. Du, Z.; He, C.; Xin, J.; Song, Z. Terahertz dynamic multichannel holograms generated by spin-multiplexing reflective metasurface. *Optics express* **2023**, *32*, 248–259.
18. Ren, B.; Tang, S.; Feng, Y.; Cui, Y.; Liu, J.; Song, J.; Jiang, Y. Dynamic and complete terahertz wavefront manipulation via an anisotropic coding metasurface. *Appl. Opt.* **2022**, *61*, 7558–7564.
19. Cao, G.; Lin, H.; Jia, B.; Yuan, X.; Somekh, M.; Wei, S. Design of a dynamic multi-topological charge graphene orbital angular momentum metalens. *Opt. Express* **2023**, *31*, 2102–2111.
20. Yao, G.; Ling, F.; Yue, J.; Luo, C.; Ji, J.; Yao, J. Dual-band tunable perfect metamaterial absorber in the THz range. *Opt. Express* **2016**, *24*, 1518–1527.
21. Cheng, Y.; Zhu, X.; Li, J.; Chen, F.; Luo, H.; Wu, L. Terahertz broadband tunable reflective cross-polarization convertor based on complementary cross-shaped graphene metasurface. *Physica E: Low-dimensional Systems and Nanostructures* **2021**, *134*, 114893.
22. Toms, N.; Chapman, J.; Ferrier, R. The application of the gerchberg-saxton algorithm to lorentz microscopy. in Electron Microscopy 1972: Proceedings of the Fifth European Congress on Electron Microscopy, University of Manchester, UK, 5-12 September 1972.
23. Ding, G.; Chen, K.; Luo, X.; Zhao, J.; Jiang, T.; Feng, Y. Dual-Helicity Decoupled Coding Metasurface for Independent Spin-to-Orbital Angular Momentum Conversion. *Phys. Rev. Appl.* **2019**, *11*, 044043.
24. Gou, Y.; Ma, H.F.; Wu, L.W.; Wang, Z.X.; Xu, P.; Cui, T.J. Broadband Spin-Selective Wavefront Manipulations Based on Pancharatnam–Berry Coding Metasurfaces. *ACS Omega* **2021**, *6*, 30019–30026.
25. Xu, J.; Liu, W.; Song, Z. Graphene-based terahertz metamirror with wavefront reconfiguration. *Opt. Express* **2021**, *29*, 39574–39585.
26. Wu, G.; Wang, W.; Zhang, R.; Yan, F.; Liang, L.; Yan, X.; Yao, H.; Wang, Z.; Li, Z.; Xu, L. Metamaterial graphene sensors for the detection of two food additives. *Opt. Express* **2023**, *31*, 32162–32171.
27. Zhu, X.; Cheng, Y.; Fan, J.; Chen, F.; Luo, H.; Wu, L. Switchable efficiency terahertz anomalous refraction and focusing based on graphene metasurface. *Diamond and Related Materials* **2022**, *121*, 108743.